ADVANCED FUNCTIONAL MATERIALS
www.afm-journal.de

Reprocessable and Mechanically Tailored Soft Architectures Through 3D Printing of Elastomeric Block Copolymers

*Alice S. Fergerson, Benjamin H. Gorse, Shawn M. Maguire, Emily C. Ostermann, and Emily C. Davidson**

Thermoplastic elastomers (TPEs) are nanostructured, melt-processable, elastomeric block copolymers. When TPEs that form cylindrical or lamellar nanostructures are macroscopically oriented, their material properties can exhibit several orders of magnitude of anisotropy. Here it is demonstrated that the flows applied during the 3D printing of a cylinder-forming TPE enable hierarchical control over material nanostructure and function. It is demonstrated that 3D printing allows for control over the extent of nanostructural and mechanical anisotropy and that thermal annealing of 3D printed structures leads to highly anisotropic properties (up to 85 × anisotropic tensile modulus). This approach is leveraged to print functional soft 3D architectures with tunable local and macroscopic mechanical responses. Further, these printed TPEs intrinsically achieve melt-reprocessability over multiple cycles, reprogrammability, and robust self-healing via a brief period of thermal annealing, enabling facile fabrication of highly tunable, robust, and recyclable soft architectures.

1. Introduction

Biological systems frequently achieve remarkable anisotropic structural and functional properties by leveraging self-assembled hierarchically ordered structures. Examples of this include incredible toughness in nacre via a staggered arrangement of individually brittle plates, remarkable flexural rigidity in bamboo achieved via controlled orientation and arrangement of cellulose fibrils and voids, and vivid structural color in species such as the Morpho butterfly.[1,2] However, few synthetic materials and manufacturing processes are capable of leveraging these hierarchical design principles, and even fewer do so with soft materials. While many synthetic materials exhibit exquisitely tailored self-assembly (including colloidal materials, block copolymers, and liquid crystalline materials), bridging their local self-assembly to large-length scales requires directed self-assembly in 3D.[3–5] Extrusion-based 3D printing is uniquely capable of acting as a form of directed self-assembly toward manufacturing tailorable 3D architected materials by controlling local structural alignment and anisotropy along arbitrary print paths.[6–13] This filament-scale structural control enables 3D printed architectures to exhibit truly hierarchical structural control, achieving tunable multiscale material properties.

Tailored architectures of mechanically anisotropic soft materials are capable of localizing strain upon deformation. Thus, they are of particular interest for applications ranging from isolating sensitive electronics within dynamic structures,[14,15] to tailoring cushioning for prosthetics, helmets, and footwear,[16–18] to achieving desirable mechanics in soft robotics applications.[19–22] Anisotropic soft inks developed to date for material extrusion are generally composed of a viscoelastic thermoset or cross–linkable elastomer matrix with an anisotropic flow- or external field-orientable filler as the source of anisotropy.[23–25] In contrast, nanostructured polymers such as block copolymers (BCPs) and liquid crystal elastomers (LCEs) inherently possess chemically tunable structural and functional anisotropy derived from a single material.[10,11,26–28] While programmed LCEs can exhibit soft tunable mechanics,[8,28] even the simplest LCEs are expensive (~$2.50/gram) and require complex processing: printing of small (typically <20 mL) batches in syringe style extruders followed by UV-induced cross–linking of extruded layers. In contrast, thermoplastic elastomers (TPEs) are an affordable (~$0.01/gram at a <50 kg scale, and less if purchased at truly bulk scales) commercially produced class of elastomeric materials comprised of ABA (glassy-rubbery-glassy) triblock copolymers which are intrinsically recyclable via melt reprocessing owing to the lack of chemical cross–linking. As block copolymers, these materials' microphases separate into ordered nanostructures as a result of the incompatibility between chemically distinct

A. S. Fergerson, S. M. Maguire, E. C. Ostermann, E. C. Davidson
Department of Chemical and Biological Engineering
Princeton University
Princeton, NJ 08540, USA
E-mail: edavidson@princeton.edu
B. H. Gorse
Department of Mechanical and Aerospace Engineering
Princeton University
Princeton, NJ 08540, USA

The ORCID identification number(s) for the author(s) of this article can be found under https://doi.org/10.1002/adfm.202411812

DOI: 10.1002/adfm.202411812

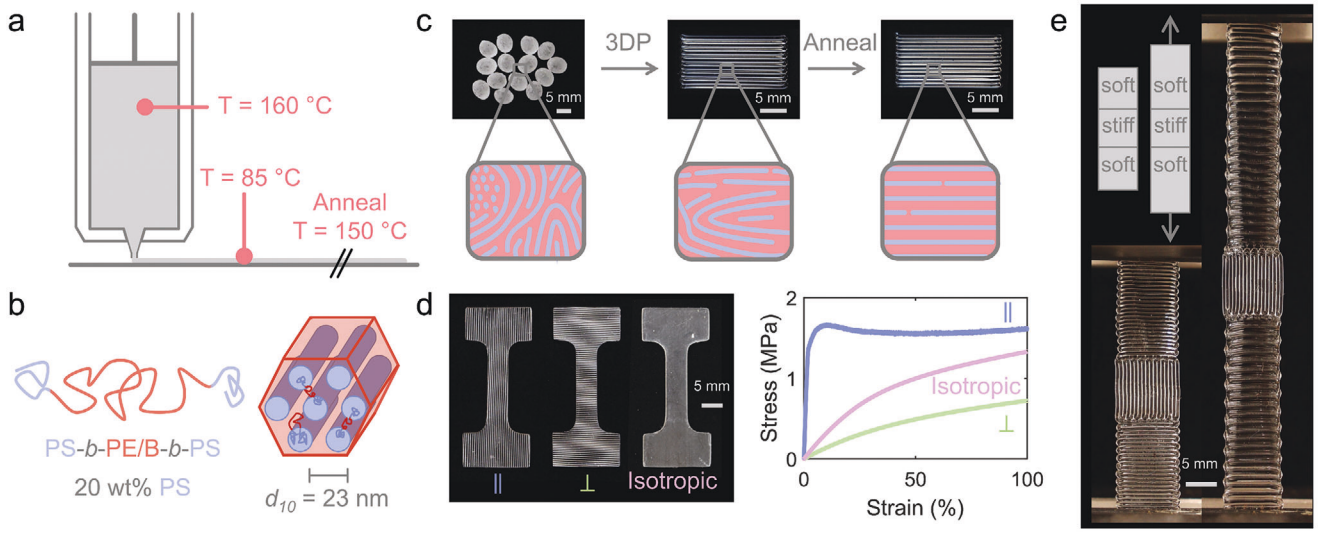

Figure 1. 3D printing-induced alignment of TPE triblock copolymers. a) Schematic of heated volumetric extruder with key processing temperatures. b) Schematics of polystyrene-*b*-poly(ethylene-co-butylene)-*b*-polystyrene (SEBS) chain architecture and micro-phase separated cylindrical nanostructure. c) Evolution of SEBS macro- and nano-scale structure throughout 3DP and thermal annealing. d) Dog-bone samples with programmed parallel and perpendicular nanostructure alignment, as well as an isotropically oriented control sample, with representative stress–strain curves. e) Programmed localized tensile response to strain in a 3D printed architecture via the organization of directionally soft and stiff regions in series.

blocks.[29–32] The most ubiquitous of these commercial materials are triblock copolymers with glassy polystyrene (PS) end blocks and either rubbery polyisoprene (PI), polyethylene/propylene (PEP), polybutadiene (PB), or polyethylene/butylene (PEB) mid-blocks. At temperatures sufficiently above the PS glass transition temperature (T_g) these materials can be melt-processed; below the PS T_g they behave as soft elastic solids. The nanostructure geometry (e.g., body-centered cubic (BCC) spheres, hexagonally close-packed (HCP) cylinders, lamellae, etc.) is determined by the relative volume fractions of each block, molecular weight, and Flory-Huggins interaction parameter between blocks.[29–32] The primary accessible geometries of interest for their anisotropic material properties are lamellae and HCP cylinders, which can exhibit up to two orders of magnitude anisotropy in mechanical properties when sufficiently oriented.[33]

For applications of interest for programmable soft architectures, manufactured objects require at minimum millimeter-scale thickness with complex spatial programming. While many studies have demonstrated surface-directed[34,35] and flow-induced alignment[36–41] in thermoplastic elastomers and the resulting anisotropic properties in macroscopically oriented samples,[42–51] existing approaches lack the ability to induce intricate, locally controllable alignment in macroscopic, 3D architectures with tunable geometries. Shear flow (both oscillatory and steady)[36,52–57] as well as extensional flow[38,39] can be employed to control TPE alignment. These principles have been leveraged by processing techniques including roll-casting from solution[40] that can induce unidirectional orientation in TPE films, as well as fabrication of unidirectionally-oriented bulk geometries through slow melt extrusion[37] or compressive "squeezing flow".[39] In contrast to these geometrically limited techniques, high operating temperature direct ink writing (HOT-DIW),[26,58] a form of material extrusion additive manufacturing,[59] is a straightforward, rapid, and scalable manufacturing technique with the ability to apply controlled shear and extensional processing flows along a programmable print path.

In this work, we leverage HOT-DIW to induce filament-scale alignment of TPE nanostructures in a commercially available cylinder forming styrenic triblock copolymer (**Figure 1**a,b). We examine the role of shear and extensional flows present during 3DP on the resulting structural and mechanical anisotropy in 3DP TPEs, as well as the key role that post-printing thermal annealing plays in improving anisotropy in these 3DP samples (Figure 1c). We demonstrate that this material exhibits near-ideal behavior for HOT-DIW, as the nanostructured TPE ink processed at these conditions intrinsically enables the formation of high aspect ratio structures, spanning structures, and unsupported overhangs. Through careful choice of print conditions followed by brief post-printing thermal annealing, we demonstrate high degrees of structural and mechanical anisotropy to both tensile and flexural deformations (Figure 1d). Additionally, we demonstrate that custom 3D printing paths allow for designer macroscopic mechanical behavior by leveraging the local programmability of BCP nanostructure alignment (Figure 1e). Finally, we note that the intrinsic melt-reprocessability and reprogrammability of these materials lead to the ability to recycle, reprogram, and self-heal damaged 3D-printed TPE objects without complex processing procedures.

2. Results and Discussion

2.1. Processing Flows in 3DP Nozzle Induce Significant Anisotropy

First, we probe the effect of forces due to flow within the nozzle (**Figure 2**a) on the resulting TPE nanostructure alignment. To quantify the effects of flow within the nozzle, we calculate the Rabinowitz corrected shear rate which describes the flow of a

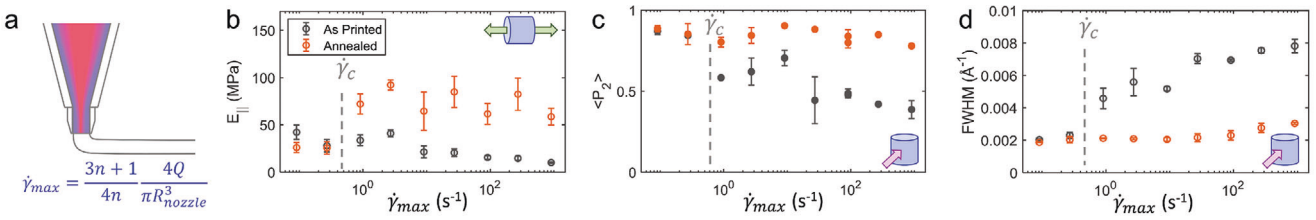

Figure 2. Impacts of printing rate on structural and mechanical anisotropy measured in individual filaments upon 3DP and subsequent thermal annealing. a) Schematic of the varied flow quantity: coupled shear (blue) and extensional (red) flow within 3DP nozzle. b) Mechanical anisotropy via $E_{||}$ and c) structural anisotropy via $<P_2>$ as a function of $\dot{\gamma}_{max}$ (at a fixed $D_R = 1$) and post-printing thermal annealing. The dotted gray line indicates a transition between distinct regimes, representing the onset of significant trapped stresses that relax upon thermal annealing. d) Full-width at half-maximum (FWHM) extracted from small-angle x-ray scattering (SAXS), indicating a transition in behavior upon thermal annealing at the critical printing rate.

shear-thinning fluid through a cylindrical capillary (Equation 1) as a measure of the maximum shear rate experienced by material inside the nozzle.[59,60]

$$\dot{\gamma}_{max} = \frac{3n+1}{4n}\frac{4Q}{\pi R^3_{nozzle}} \quad (1)$$

This quantity depends on the volumetric flow rate Q, nozzle exit radius R_{nozzle}, and a power law shear-thinning exponent n, which we obtained as 0.81 from fitting to rheological data (Figure S1, Supporting Informationf). Translational print speeds and corresponding volumetric extrusion rates corresponding to the range of shear rates probed in this study are detailed in Figure S2, Supporting Information. While Equation 1 is only rigorous in the case of fully developed flow within the cylindrical capillary, the calculated $\dot{\gamma}_{max}$ remains a helpful (but not strictly quantitative) quantity to parameterize the flow. Here, $\dot{\gamma}_{max}$ is primarily controlled by varying both Q and R_{nozzle}. Although we quantify the effects of the flow within the nozzle using a measure of the shear rate, it is critical to note that the extrudate experiences a complex flow profile with a significant extensional component within the nozzle, particularly along the centerline in the converging region. Thus, as the volumetric flow rate increases, the magnitude of shear and extensional flow rates within the nozzle increase in tandem. As such, $\dot{\gamma}_{max}$ should be taken as a proxy for the coupled shear and extensional flows within the nozzle, since both components of the flow will be strongly impacted by both Q and R_{nozzle}.

In order to quantify the effects of these 3DP processing flows, we use two primary techniques to quantify the structural and mechanical anisotropy that results from 3DP of single TPE filaments. First, 2D small-angle X-ray scattering collected with the X-ray beam perpendicular to the filament axis probes the extent of alignment of cylindrical nanostructures along the filament axis. From these data, we extract an orientational order parameter $<P_2>$ as a convenient measure of the overall extent of unidirectional alignment of the TPE nanostructures within 3D printed filaments, calculated from the angular (χ) distribution of scattering intensity (Equation 2).

$$\langle P_2 \rangle = \frac{3\langle cos^2\chi \rangle - 1}{2} \quad (2)$$

This orientational order parameter has an embedded assumption that the object possesses cylindrical symmetry;[61,62] here, this assumption is reasonable due to the uniaxial symmetry of the flow profile within the nozzle. Note that $<P_2>$ is calculated from the primary SAXS peak, which corresponds to lateral cylinder-cylinder correlations.

Secondly, tensile testing probes the extent of both nanostructure alignment and glassy PS domain continuity within printed filaments. To quantify mechanical anisotropy isolated from print path effects, we report the small-strain modulus of single printed filaments measured along the print direction, $E_{||}$. Tensile testing performed on sheets of printed material yield perpendicular small-strain moduli ($E_{\perp}$) over a narrow range between 1.2-2.2 MPa with no systematic dependence on printing conditions or thermal annealing history (Figure S3, Supporting Information). Therefore, while the single filament geometry is not conducive to tensile measurements perpendicular to the print path (and thus we do not report $E_{\perp}/E_{||}$ directly for single filaments), our data supports that $E_{||}$ is an appropriate proxy for the mechanical anisotropy of a sample. It is critical to emphasize that the modulus of an oriented sample strained parallel to the alignment axis is dependent on both PS domain alignment and long-range PS domain continuity. In contrast, an oriented sample strained perpendicular to the alignment axis initially deforms via distortion of the PS cylinder lattice, a mechanism that has been discussed in detail in foundational TPE alignment studies and via in-situ scattering,[33,43,63,64] and is not intrinsically sensitive to PS domain continuity or defect density. Beyond a certain limit, X-ray scattering is not informative concerning PS domain continuity or defect density.[65] While the FWHM from X-ray scattering can be informative regarding domain size in the cylinder-cylinder correlation direction, the measurement provides no information regarding domain size along the cylinder axis; it is this latter size that dominates the tensile mechanics of our materials in the parallel configuration. As such, X-ray scattering and small-strain tensile testing probe distinct and complementary aspects of aligned 3D printed samples.

With these characterization methods, we find that samples printed with increasing $\dot{\gamma}_{max}$ exhibit a decrease in measures of both structural (Figure 2b) and mechanical (Figure 2c) anisotropy upon 3D printing. Alone these results may suggest a decrease in the extent of alignment induced by such printing conditions. However, we find that for all samples printed at or above a critical shear rate $\dot{\gamma}_c \approx 1\ s^{-1}$, thermal annealing at 150 °C for 10 min after 3D printing results in a significant increase in measures of both structural and mechanical anisotropy. Annealed samples display $<P_2>$ and $E_{||}$ ranging between 0.75–0.92 and 50–100 MPa

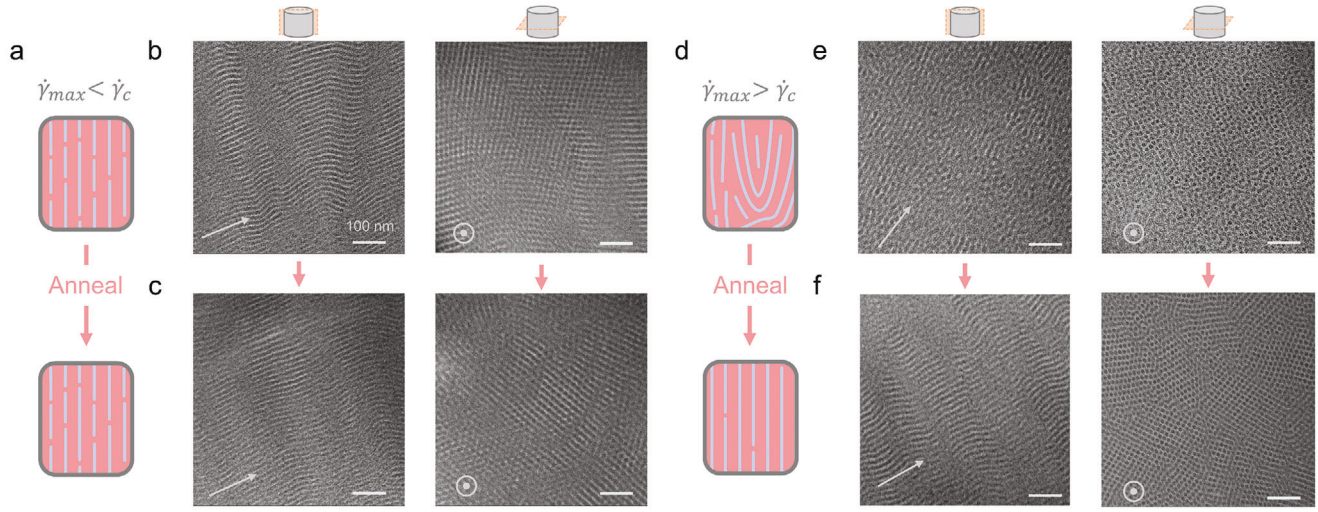

Figure 3. Schematics and TEM images of SEBS nanostructures evolution upon 3D printing and thermal annealing at two printing conditions. a) Schematic of nanostructure evolution upon thermal annealing in samples printed below $\dot{\gamma}_c$, exhibiting minimal relaxation of trapped stresses upon thermal annealing. TEM images of samples printed at $\dot{\gamma}_{max} = 0.09\ s^{-1}$ upon 3D printing (b) and after thermal annealing (c). d) Schematic of nanostructure evolution upon thermal annealing in samples printed above $\dot{\gamma}_c$, exhibiting significant relaxation of trapped stresses upon thermal annealing. TEM images of samples printed at $\dot{\gamma}_{max} = 90\ s^{-1}$ upon 3D printing (e) and (f) after thermal annealing. The approximate print direction is denoted by an arrow in each image. Side-on views of PS domain geometry and continuity (left) and end-on views of PS cylinder cross-sections (right) are included.

respectively. The nature of this increase in anisotropy is intriguing since thermal annealing does not itself provide a driving force to induce alignment. As such, the increase in anisotropy observed upon annealing must result from structural rearrangements and/or relaxations of trapped stresses in an aligned but defect-heavy nanostructure (**Figure 3d**). This is supported by transmission electron microscopy (TEM) imaging of high $\dot{\gamma}_{max}$ samples before and after thermal annealing (Figure 3e,f). Before annealing we observe a clear lack of long-range domain continuity and nanostructure ordering, whereas after thermal annealing we observe a high degree of long-range PS domain continuity and a highly regular ordered nanostructure. This is additionally supported by the decrease in the FWHM of the primary SAXS peak of high $\dot{\gamma}_{max}$ samples upon thermal annealing (Figure 2d).

We observe a deviation from the previously discussed behavior in the lowest range of shear rates probed in this study. Samples printed below $\dot{\gamma}_c$ exhibit no significant change in either structural or mechanical anisotropy upon annealing, and SAXS analysis reveals decreases in domain spacing but no significant change to the FWHM upon thermal annealing (Figure S4d,j, Supporting Information). These features in the SAXS patterns indicate that thermally annealing these samples leads to a relaxation of a deformed but well-ordered nanostructure. This is in contrast with samples printed well above the $\dot{\gamma}_c$ transition, which exhibit no change in domain spacing upon thermal annealing. Samples printed below this transition also exhibit a significantly lower degree of mechanical anisotropy after annealing ($E_{\parallel}$ = 25.5 MPa), compared to samples printed above $\dot{\gamma}_c$ ($E_{\parallel}$ > 50 MPa). This drastic difference in $E_{\parallel}$ despite effectively identical $<P_2>$ indicates that the nanostructure is similarly aligned along the print path, but even after thermal annealing lacks the long-range PS domain continuity required to display similarly increased moduli (Figure 3a). TEM imaging of these samples both before and after thermal annealing confirms the presence of well-defined hexagonal ordering of PS cylinders both before and after annealing, with minimal observable changes upon annealing (Figure 3b,c). Unfortunately, our current characterization approaches appear incapable of directly probing the critical PS cylinder length which is necessary to achieve outstanding tensile moduli.

The presence of this transition in anisotropy and response to thermal annealing suggests the presence of a critical shear rate and/or extensional strain rate associated with this $\dot{\gamma}_c$ threshold, above which a critical chain and/or nanostructure relaxation is unable to occur on the timescale of 3D printing. Based on the structural and mechanical anisotropy observed in printed and annealed samples, this relaxation upon thermal annealing must lead to a greater degree of long-range PS cylinder continuity and therefore a reduction in the number of mechanically ineffective defects in samples printed above this $\dot{\gamma}_c$ threshold.

2.2. Post-Extrusion Extensional Flow Maximizes Anisotropy

Next, we investigate the impacts of nearly isolated extensional flow by filament drawing during deposition. By translating the nozzle at a velocity greater than the average material velocity thro, we obtain "highly drawn" filaments with cross-sectional areas smaller than that of the nozzle. We quantify the magnitude of this extensional flow via the ratio of nozzle translation and average material velocities, or of the cross-sectional areas of the nozzle, A_{nozzle}, and the deposited filament, $A_{filament}$ (**Equation 3**).[66–68] Experimentally, this is achieved by extruding at a fixed volumetric flow rate and increasing the translational velocity from v_0, which produces a filament equal in diameter to the nozzle, to v_{nozzle}, which produces a filament smaller in diameter than

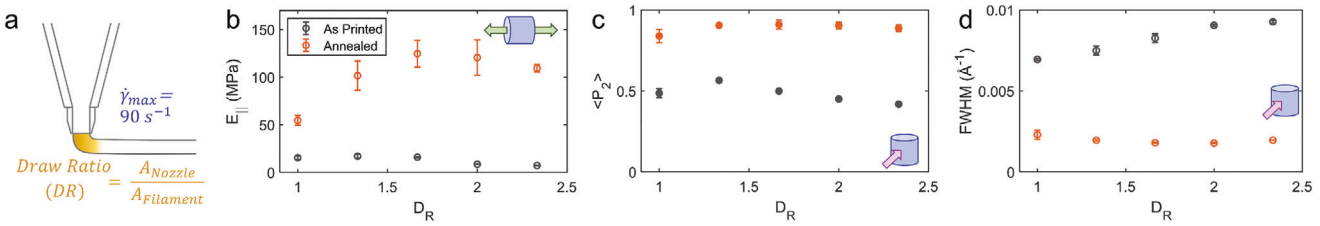

Figure 4. Impacts of extension via draw ratio on structural and mechanical anisotropy measured in individual filaments upon 3DP and subsequent thermal annealing. a) Schematic of the varied flow quantity: isolated extensional (yellow) flow upon deposition onto a substrate. b) Mechanical anisotropy via $E_{||}$ and c) structural anisotropy via $<P_2>$ as a function of D_R (at a fixed $\dot{\gamma}_{max} = 90\ s^{-1}$) and post-printing thermal annealing. d) FWHM extracted from SAXS, indicating a larger magnitude of nanostructure rearrangement upon thermal annealing at higher draw ratio conditions.

the nozzle, a process which is commonly referred to as under extrusion.

$$D_R = \frac{A_{nozzle}}{A_{filament}} = \frac{v_{nozzle}}{v_0} \text{ at fixed } Q \quad (3)$$

This form of applied extension imparts nearly uniform extensional flow across the entire deposited filament, and varying the draw ratio adjusts the effective strain rate and net extensional strain experienced by the entire filament prior to deposition. This is in contrast with other sources of extensional flow in 3DP where the extension is highly localized, such as the extensional flow within the nozzle centerline, or the extensional flow associated with the 90° turn during material extrusion printing which is concentrated in the lower region of a deposited filament.[69] We do not explore these latter extensional effects in this work: the former extensional flow cannot be uniquely decoupled from the shear flow within the nozzle without tuning nozzle geometry while examining the latter would require controlling the tilt angle of the nozzle relative to the substrate, which is outside the scope of this work. We further note that direct ink write (DIW) 3D printing methods, such as our technique, typically deposit near-cylindrical roads which results in a distinct flow history from most commercial fused-filament fabrication (FFF) printing methods which deposit thin and wide roads, leading to additional shearing of the material along the print path. Here we do not attempt to directly apply FFF print path conditions in our process, though the effects of the distinct flow history may be of interest for future study.

We find that applying this nearly pure extensional flow (**Figure 4a**) by increasing the draw ratio provides the most effective means of achieving a high degree of mechanical anisotropy in 3D-printed TPEs. Samples printed with $D_R > 1$ (with a fixed $\dot{\gamma}_{max} = 90\ s^{-1}$, chosen to facilitate rapid sample fabrication) display little effect of D_R on anisotropy immediately upon printing, but recovers very high values of structural (Figure 4c) and mechanical (Figure 4b) anisotropy upon thermal annealing, with $<P_2> \approx 0.90$ and $E_{||} > 100$ MPa. Similar to the un-drawn samples printed at this $\dot{\gamma}_{max}$, these high D_R samples also display a significant decrease in FWHM of the primary scattering peak observed via SAXS (Figure 4d). Similar trends in $<P_2>$ and FWHM with respect to D_R are observed for a series printed at a moderate $\dot{\gamma}_{max}$ ($2.7\ s^{-1}$) which is only slightly above the $\dot{\gamma}_c$ threshold (Figure S4f, Supporting Information). To date we have not characterized the effects of extension below the $\dot{\gamma}_c$ threshold due to the impractically long timescales required to print structures at these conditions.

There are several potential causes for the increase in alignment upon annealing observed in samples printed at high draw ratios ($D_R > 1$). The increased structural and mechanical anisotropy observed in annealed high D_R samples may be attributable to the fact that the extensional forces applied to the material via "drawing" are distributed across the entire cross-sectional area of the filament. This is in contrast with the extensional flow inside the nozzle, which is expected to be spatially varied and concentrated along the centerline of the nozzle. It is possible that extensional flow is the dominant factor in inducing a high degree of structural and mechanical anisotropy across all samples in this work,[38,39] and the increased anisotropy observed in high D_R samples is reflective of the higher proportion of extension in the material flow history. Another notable difference between the in-nozzle and post-extrusion extensional flows is the temperature at which the extensional flow occurs. Extension occurring within the 3DP nozzle is occurring at or near the measured nozzle temperature of 160 °C which is well above the PS block T_g (Figure S5, Supporting Information), while the extension applied by drawing is occurring as the material is rapidly cooling down upon exposure to a near-T_g substrate and the surrounding ambient air. The limited PS chain mobility associated with the proximity to the glass transition during this extensional flow may account for a greater magnitude of unrelaxed stresses being trapped in the extrudate upon 3D printing, resulting in a more significant nanostructural rearrangement toward a higher population of long-range continuous PS cylinders upon thermal annealing.

The increased mechanical anisotropy induced by annealing highly drawn filaments is accompanied by additional nanostructural changes upon annealing. SAXS analysis of the D_R series at both high ($90\ s^{-1}$) and moderate ($2.7\ s^{-1}$) $\dot{\gamma}_{max}$ reveals trends similar to those observed in high $\dot{\gamma}_{max}$ samples without drawing: the primary scattering peak does not shift upon annealing while the FWHM decreases, corresponding to a transition from an aligned but highly defect-heavy nanostructure to a well-oriented nanostructure comprised of high aspect ratio PS cylinders(Figure S4h,i,k,l, Supporting Information). We note that all highly drawn samples exhibit a slight decrease in the post-annealing domain spacing compared to the un-drawn ($D_R = 1$) samples (Figure S4h,i, Supporting Information), which is consistent with findings previously reported for how cylindrical SEBS

nanostructures relax after being exposed to uniaxial extension in the melt state.[38,70,71]

2.3. 3D printing of Styrenic BCPs Enables the Facile Fabrication of Complex Architectures

In order to effectively leverage these anisotropic properties in printed architectures, we must ensure that the material is compatible with printing well-defined, controlled structures. In order for a material to be 3D printable using extrusion-based techniques, it must meet several rheological criteria.[59] These criteria include shear-thinning behavior to facilitate flow within the nozzle, while a higher effective viscosity and/or the presence of sufficient yield stress allows for the material to effectively solidify upon deposition to preserve the intended structure and physically support additional layers without deforming. When 3DP inks do not possess a true yield stress they are poorly suited to generating spanning structures, unsupported overhangs, or supporting many layers without sagging. Melt-extrusion of TPEs, specifically onto a near-T_g substrate, meets these rheological requirements very well due to the shear-thinning behavior observed in the melt state (Figure S1, Supporting Information) as well as the presence of a true yield stress (Figure S6, Supporting Information) resulting from the microphase separated nanostructure geometry.[38,60,72,73] These rheological features are characteristic of materials that are well-suited to melt-extrusion 3D printing.

We demonstrate that these rheological properties result in highly successful performance in HOT-DIW 3D printing through the material's ability to achieve several representative "challenging" DIW structures. In a classic log-pile structure (**Figure 5**a), we observe minimal sagging of spanning structures, indicating that these 3DP SEBS filaments can effectively span gaps of 10x the filament diameter. We fabricate a high aspect ratio vase (Figure 5b) to demonstrate the ability to print many (60+) layers without any significant sagging and to demonstrate the material's ability to accommodate printing moderate overhangs of unsupported material. Additionally, we demonstrate our ability to easily incorporate functional additive materials into the 3DP ink, such as perdeuterated contorted hexabenzocoronene (d_{24}-cHBC), an organic molecule that exhibits long-lived (>20s) red phosphorescence upon relaxation following UV-excitation.[74] We fabricate flower shapes from the yellow-colored 0.5 wt.% d_{24}-cHBC in the SEBS composite and show that the emission properties are maintained in the 3DP composite (Figure 5c). We also demonstrate high print path fidelity through multiple layers in more complex geometric print paths including sharp turns via the fabrication of a well-resolved multi-layer text object reading "Princeton" (Figure 5d).

Additionally, the presence of a yield stress in these triblock thermoplastic elastomers in the melt uniquely facilitates thermal annealing to both improve interface quality (Figure S7, Supporting Information) and increase mechanical anisotropy without deformation or loss of resolution in the 3D printed structure. Traditional 3D printed structures frequently suffer from poor interfacial mechanics due to the incompatibility of traditional thermoplastics such as ABS and PLA with such a post-printing thermal annealing step. Without such a processing step to allow for adequate polymer chain diffusion and formation of entanglements

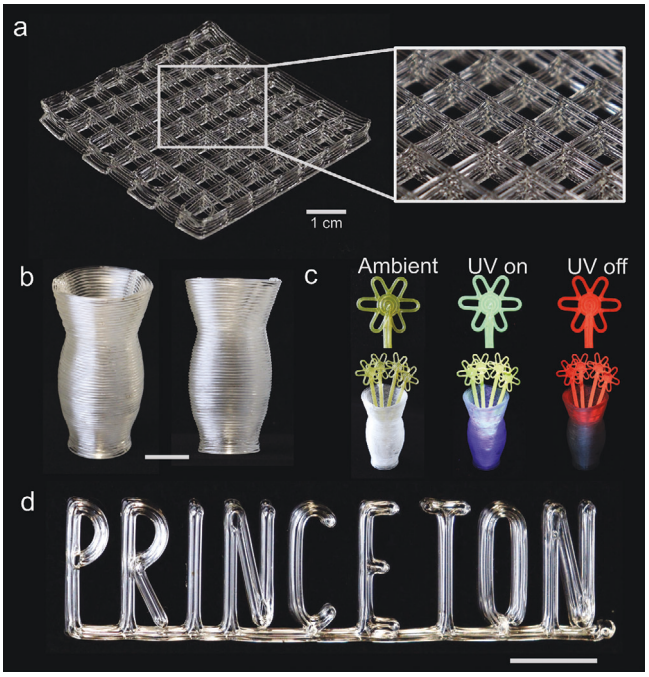

Figure 5. 3DP SEBS structures achieve a high degree of print path fidelity and can achieve desirable structural characteristics. a) 3DP log-pile structure demonstrating the ability to produce spanning structures without sagging. b) 3DP vases demonstrate the ability to produce high aspect ratio structures without lower layers collapsing, as well as moderate unsupported overhangs. c) 3DP SEBS/d_{24}-cHBC composite flowers inside 3DP SEBS vase, demonstrating incorporation of functional additives. Here the yellow-colored small molecule is excited by UV-excitation and exhibits long-lived (>20 sec) red emission after UV exposure stops. d) 3DP "Princeton" text displaying high print path fidelity maintained over 5 layers, including in difficult print path scenarios such as U-turns and right angles.

across filament interfaces, there are few simple methods to improve the mechanics of traditional 3D printed parts.[75] The ability to thermally anneal these TPEs above T_g to improve the interfacial properties of 3D printed architectures without any loss of programmed structure or function is a distinct advantage of this class of materials.

2.4. Programmable Anisotropy Enables Tailored Mechanical Functionality

Next, we demonstrate that our ability to control material properties along a print path enables the fabrication of soft architectures tailored to exhibit controlled mechanical functionality such as controlled localization of tensile and flexural deformation. We fabricate several representative mechanically functional architectures using fixed $\dot{\gamma}_{max} = 90\ s^{-1}$ and $D_R = 1.67$ printing condition. Here we use a single printing condition because it is straightforward to encode when manually designing print paths, though the printing condition can additionally be varied throughout an architecture to provide an additional level of tunability beyond solely customizing the print path.

First, we demonstrate that tensile strain isolation and tunable strain distribution within a printed object can be programmed by organizing stiff and soft segments of a strip in series (**Figure 6**a),

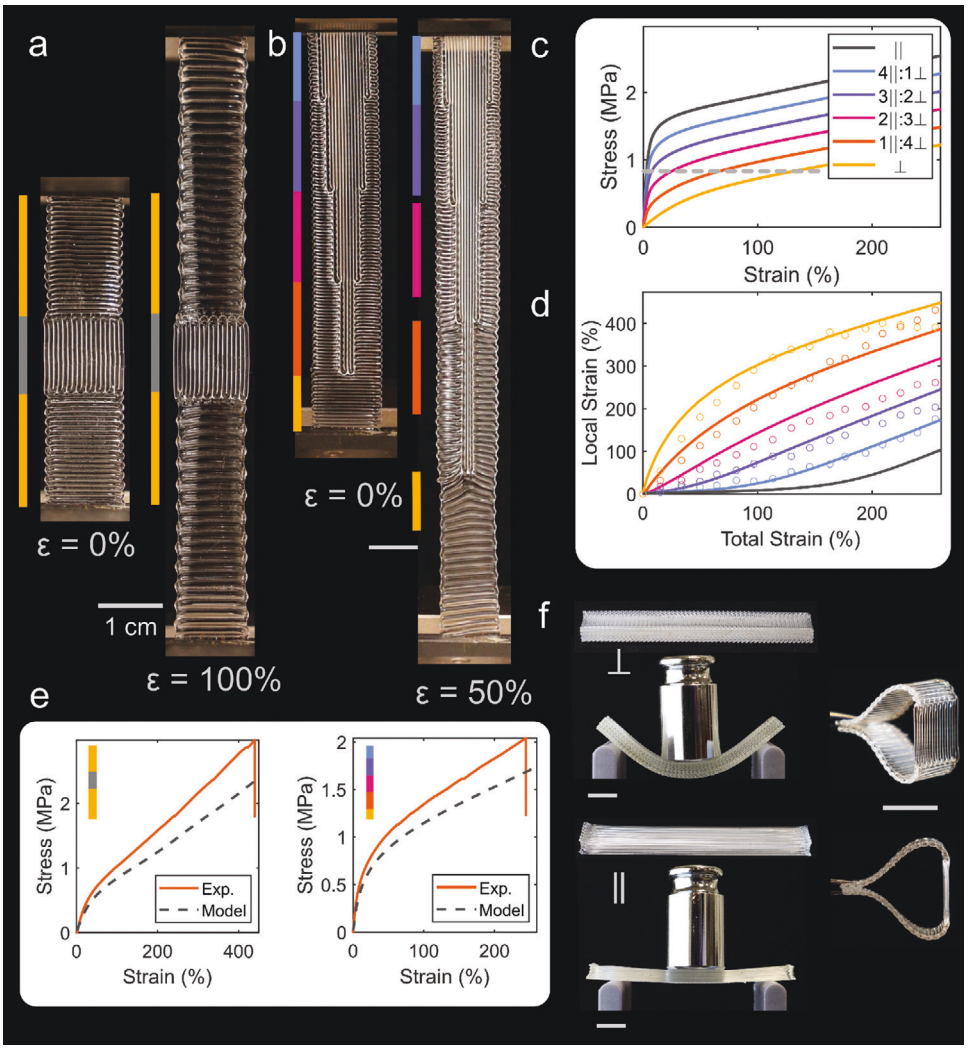

Figure 6. Tailored macroscopic mechanical functionality in 3DP TPEs via controlled print paths. a) Tensile strain isolation obtained in a three-segment strip by organizing directionally soft and stiff components in series. b) Further controlled strain localization in a five-segment strip by organizing soft and stiff components in series and in parallel. c) Predicted stress–strain curves for each of the "segments" of the sample in (b), defined by the ratio of material composed of parallel and perpendicular print paths. The dotted grey line is a "tie line" at representative stress: its intersections with each stress–strain curve indicate that segment's expected local strain. d) Localization of strain to each segment within the architecture in (b). Solid lines represent model predictions and circles represent experimental data obtained via image analysis during deformation. e) Overall stress–strain curves for the architectures in (a) and (b), along with model predictions. f) Flexural anisotropy achieved in 3DP TPEs demonstrated via the varying degree of bending under loading of 100 g weight as a function of print path (left) and the flexural strain isolation behavior achieved using the architecture in (a).

or a combination of stiff and soft segments both in series and in parallel (Figure 6b). When strain is applied along the intended deformation direction, the engineering stress is uniform across the length of these architectures, but strain concentrates in the softer segments due to the lower effective modulus. For a sample with segments of varied stiffness organized in series as in Figure 6a, the stiffer segment retains the original dimensions (straining less than 2%) until the soft segments reach ≈225% strain. At this point, the engineering stress reaches the yield stress of the parallel-oriented stiff segment,1.15 MPa (Figure S8, Supporting Information), and more significant deformation of the stiff segment is induced (Video S1, Supporting Information). A sample with stiff and soft segments organized both in series and in parallel as in Figure 6b results in an architecture with graded mechanical properties. Segments containing larger proportions of stiff filament orientations have a higher value of their effective yield stress and effective modulus, leading to staged yielding and tunable distribution of strain localization (Video S2, Supporting Information).

Further, we can model the predicted mechanical performance and strain isolation functionality of such architectures composed of stiffer and softer components organized in series and parallel as discussed. The predicted stress–strain curves of each segment within the architecture in Figure 6b (stiff and soft components in parallel) are calculated via a linear combination of the parallel and perpendicular stress–strain curves since deformation in parallel requires constant strain across all components (Figure 6c). With the predicted stress–strain properties of these segments which

are then oriented in series within the architecture in Figure 6b, we can further predict the localization of strain throughout the architecture. Deformation in series is subject to a constant stress restriction and as such, a horizontal constant stress tie-line as is shown in Figure 6c intersects with the stress–strain curves for each segment at the expected value of local strain within that segment. By extracting these intersection points across a range of stresses, we obtain the distinct deformation trajectories of these mechanically graded segments as a function of the total strain applied to the sample (Figure 6d). The experimental data extracted from image analysis during the deformation of the architecture in Figure 6b follow the expected strain localization trajectories in Figure 6d quite well. Some deviation is observed, particularly in the softer segments, which we expect may be a result of print path effects such as corners which are likely to have a slight stiffening effect and are not accounted for in this model, as the input stress–strain curves to this model were obtained using samples without edge effects. Further characterization of such print path effects may be of interest for future study if quantitative predictive modeling of the resulting strain localization properties is desired, but is outside the scope of this work. This model additionally enables approximate prediction of the overall stress–strain curve of these tunable soft architectures (Figure 6e). We expect that the slight under-prediction of the stress during deformation is a result of previously discussed print-path effects such as corners, slight defects at overlapping regions between stiff and soft print paths, as well as additional stress concentration at interfaces between mechanically distinct segments. During straining, a highly deformed segment will have a large decrease in cross–sectional area while being attached to a segment with either no or minimal change to cross-sectional area, leading to an interfacial region of stress concentration, non-uniform deformation, or sample bowing at these interfaces, as can be seen in Figure 6a,b and may account for deviations in overall stress–strain behavior from the model predictions.

In addition to programmable behavior in response to tensile strain, these architectures also exhibit highly anisotropic flexural behavior (Figure 6f). Bending moduli of 2.48 ± 0.11 and 1.07 ± 0.09 MPa were measured via single-cantilever dynamic mechanical analysis (DMA) measurements for samples fabricated with the print direction along and perpendicular to the long axis of the test specimen, respectively. This flexural anisotropy can be leveraged to localize bending in these types of soft architectures (Figure 6f). While 3DP samples display some of this mechanical anisotropy before thermal annealing, the extent of tensile and flexural strain isolation is greatly enhanced by thermal annealing (Figure S9, Supporting Information) and is, therefore, a critically important processing step in fabricating these functional soft architectures. Ultimately, we envision that these strain isolation capabilities can be leveraged for applications such as housing delicate components and electronics in strain-isolated regions of wearable devices.

2.5. TPEs are Inherently Recyclable and Reprocessable Materials

Finally, we demonstrate the ability to maintain the programmed mechanical function for multiple cycles, even after straining beyond the point of softening due to PS cylinder breakup.

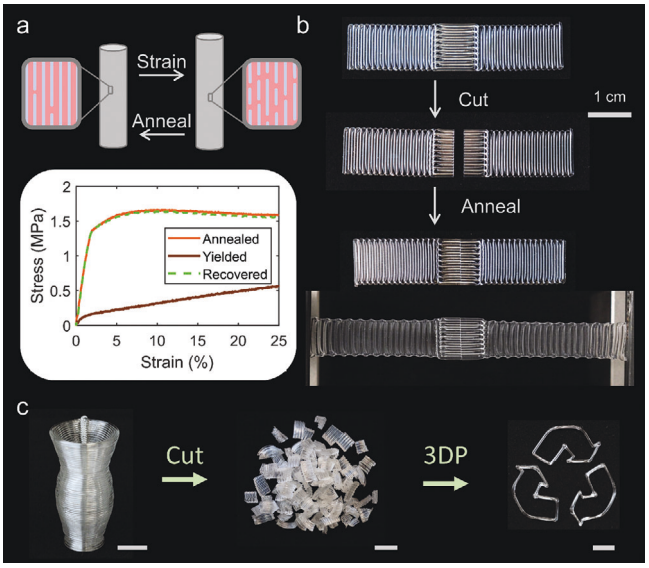

Figure 7. Recyclability and reprocessability of TPEs in 3DP. a) Recoverability of mechanical anisotropy via thermal annealing after samples have been strained beyond yielding. b) Self-healing behavior of TPEs, achieved via thermal annealing. c) Reprocessability of TPEs for 3D printing.

As previously discussed, the stiffness of an oriented styrenic TPE is governed by both PS domain alignment and long-range continuity.[33,43,76] As such, an appropriately oriented sample may exhibit a high small strain modulus ($E_{\parallel} > E_{iso} = 3.2$ MPa) in the direction of alignment before yielding on the first strain cycle, but will exhibit a low small strain modulus (approx. $= E_{iso}$) on all subsequent straining cycles. However, straining to a point between yielding ($\varepsilon \approx 2\%$) and fracture ($\varepsilon \approx 1000\%$) results in the breakup of PS cylinders without permanent disruption of the alignment of the PS domain segments after the strain is released.[43,48] Thermal annealing of these yielded 3D printed samples allows sufficient mobility of PS chains to weld the interfaces between broken PS domains to recover long-range domain continuity and the associated first-cycle mechanical properties. This recovery of properties has been previously demonstrated in bulk-oriented TPE samples,[43] and allows us to easily recover the programmed mechanical function after cylinder breakup due to straining in our 3D-printed soft architectures. We observe no significant difference between the modulus of an annealed sample and of a sample that has been "damaged" via straining beyond yielding and then "recovered" by thermal annealing at the same thermal conditions described previously (**Figure 7a**).

Additionally, 3D-printed TPEs that have been broken or cut can self-heal upon a brief thermal anneal. TPEs have previously been demonstrated as a source of self-healing behavior in soft robots.[77] Here we demonstrate that when our 3D-printed TPEs are cut and self-healed via a brief thermal annealing step (10 min. at 150 °C), the initially programmed mechanical anisotropy is maintained in the healed object (Figure 7b). This thermal annealing provides sufficient mobility for PS cylinders to regain domain connectivity across the cut interface, ultimately recovering the long-range PS domain continuity required for improved stiffness along the programmed direction of alignment.

A further intrinsic advantage of these thermoplastic elastomers for 3D printing is the inherent melt reprocessability and recyclability. Traditional elastomers are chemically cross–linked, and therefore are not recyclable. Significant effort in recent years has gone into developing chemically recyclable elastomer networks[78–80] and resins for 3D printing applications.[81,82] However, these methods are frequently expensive, synthetically challenging, and/or exhibit considerable degradation of properties upon recycling. In contrast, thermoplastic elastomers offer multicycle melt reprocessability (Figure 6c) and reprogrammability without loss of achievable anisotropy (Figure S10, Supporting Information), as well as the previously discussed self-healing behavior.[77] We have not observed significant degradation of achievable functional anisotropy resulting from reprocessing these TPEs, suggesting minimal processing-induced degradation via chain scission or oxidation occurs, which we confirm via gel permeation chromatography (GPC) analysis (Figure S10, Supporting Information). We acknowledge that this particular SEBS composition has a relatively low molecular weight and a fully hydrogenated rubbery block, and note that higher molecular weight and non-hydrogenated chemistries may be prone to some degradation upon processing. However, the lack of degradation in this SEBS species is promising regarding leveraging this class of materials in 3D printing. Ultimately these reprocessability and self-healing benefits are inherent to nanostructured thermoplastic elastomers without any additional chemical functionalization or complex processing steps, making these materials prime candidates for many scalable applications of interest.

3. Conclusions

In this work, we have demonstrated the ability to controllably induce structural and mechanical anisotropy in commercial thermoplastic elastomers by varying easily controllable 3D printing parameters. We have identified 3D printing conditions in which significant structural rearrangement and an increase in anisotropic material properties occur upon post-printing thermal annealing. Additionally, we have shown that the application of isolated extensional forces by drawing the material upon deposition provides the most effective and consistent control over material anisotropy in this system. We have demonstrated effective fabrication of complex geometries with high print path fidelity, and have achieved tailorable mechanical properties in custom soft architectures through tailored print paths. Ultimately this work introduces a straightforward and highly scalable fabrication technique leveraging commercially available TPEs as intrinsically anisotropic nanostructured materials which are inherently recyclable and reprogrammable. We anticipate that this approach will enable the fabrication of highly tunable soft architectures that are compatible with custom human-interfacing devices such as consumer electronics or wearable biomedical devices and are fundamentally compatible with a wide range of functional block copolymers, enabling a broad range of potential applications.

4. Experimental Section

SEBS Characterization: The triblock copolymer, Kraton MD1648, was provided by Kraton in the form of dense pellets and was used as received. Gel permeation chromatography was run on a PSS SDV analytical 1000 Å column with a THF flow rate of 0.3 mL mi^{-1}n, using a refractive index detector. GPC analysis provided M_n = 43.6 kg mol^{-1} and Đ = 1.02 with respect to PS standards (Figure S11, Supporting Information). The styrene content was determined to be 19.4 wt.% according to ^{1}H-NMR analysis. NMR was performed in a 500 MHz Bruker spectrometer with a 10 s relaxation delay (Figure S12, Supporting Information). Differential scanning calorimetry, run from −80 to 150 °C at 2 °C min^{-1} on a TA-DSC2500 indicated glass transition temperatures of −45 °C and ≈62 °C for PEB and PS blocks respectively (Figure S5, Supporting Information). Small-angle X-ray scattering of a sample slowly cooled from above T_{ODT} indicates that the equilibrium nanostructure takes the form of a hexagonal lattice of cylinders with an equilibrium domain spacing of 20 nm between {10} planes (d_{10} = 20 nm) as received (Figure S13, Supporting Information), and remains hexagonal at all processing conditions used in this work (Figures S14 and 15, Supporting Information). Globally isotropic control samples of ≈0.5 mm thickness for mechanical analysis and for rheological studies were prepared by cooling SEBS from above T_{ODT} using a Carver hot press. Rheological characterization was performed on an Anton Paar MCR 302e using a 25 mm parallel plate configuration with a gap height of 0.385 mm. A steady shear-rate sweep from 0.01–100 s^{-1} yielded a shear thinning exponent n = 0.81 (Figure S1, Supporting Information). Oscillatory strain amplitude sweeps from 0.1–10% at a fixed frequency ω = 0.03 rad s^{-1} allowed for characterization of the yield-stress behavior at the extrusion temperature (Figure S6, Supporting Information).

3D Printing: 3D printing was carried out using a custom heated volumetric extruder. A 50 mL capacity stainless steel reservoir with a 20 mm inner diameter was mounted in a custom machined aluminum block fitted with two 300 W (91 W in^{-2}) heating cartridges (McMaster). Temperature control was achieved using a PID controller (Inkbird 106VH) and a k-type M3 screw thermocouple (uxcell) fitted adjacent to the nozzle (Figure S16, Supporting Information). The nozzle temperature was set to 160 °C to facilitate the extrusion of a smooth filament and avoid melt-flow instabilities at targeted extrusion rates (Figure S17, Supporting Information). The nozzle temperature was allowed to stabilize to within 1 °C for at least 15 min before use. Temperature fluctuations during printing were minimal (<1 °C). Volumetric extrusion was controlled by activating a NEMA 17 stepper motor (StepperOnline) to drive a lead-screw-mounted custom-machined stainless-steel plunger fitted with a rigid Teflon O-ring (McMaster) through the reservoir. Custom M6 threaded Arque style nozzles (Tecdia) with 250 and 700 µm inner diameters were fitted to the end of the reservoir for extrusion.

The extruder assembly was mounted to a set of controlled motion axes (Aerotech). Communications with the stepper motor and all motion axes were controlled through the instrument software (Aerotech A3200). Samples were 3D printed onto 1 mm × 25 mm × 75 mm microscope slides (VWR) or ⅛″ borosilicate glass substrates (McMaster) as dictated by overall sample dimensions. Glass printing substrates were secured on a leveled low-profile hot plate (Wenesco) set to 90 °C. The actual substrate temperature was 85 °C, as verified by IR thermometer and k-type thermocouple readings. This substrate temperature was chosen as the minimum temperature required which allows sufficient sample adhesion during and following turns (Figure S18, Supporting Information).

Select low shear rate samples requiring extremely long (>6 h) print times were fabricated using a HYREL Engine SR equipped with a TAM head and HTK-270 high temperature, high torque compatible reservoir. The reservoir was fitted with the previously described custom Tecdia nozzles for extrusion and had a capacity of ≈2 mL. Reservoir and print bed temperatures were calibrated such that the nozzle and substrate temperatures were within 2 °C of the previously described 3D printer assembly. G-code commands run on this instrument were written manually such that all translational speeds and material extrusion rates were identical to parameters used on the Aerotech system.

For the red-light emitting SEBS/d_{24}-cHBC 3D printed flowers, SEBS pellets were melt-compounded with 0.5 wt.% perdeuterated contorted hexabenzocoronene powder (synthesized by M.R. Ivancevic).[74] This was done by melt-pressing the two components between Teflon sheets at 150 °C, manually compressing the resulting sheet into a ball, and melt-pressing again a total of 8 times to ensure homogeneity. The mixture was

3D printed using $\dot{\gamma}_{max} = 27\ s^{-1}$ and $D_R = 1$ as printing conditions, additionally using poly(vinyl-alcohol) (Sigma Aldritch coated glass slides as substrates to improve adhesion. 3D printing was performed using the HYREL reservoir custom-mounted on the Aerotech axes and controlled similarly to the fully custom extruder.

Sample Preparation: 3D printing nozzle velocities and volumetric extrusion rates were varied from 0.0075–18 mm s^{-1} and 0.00289–2.89 $mm^3\ s^{-1}$ in order to achieve the desired draw ratio (D_R) and maximum shear rate $\dot{\gamma}_{max}$ (Equation 1,3). Generalized print path parameters were determined as a function of theoretical filament diameter ($D_{fil,\ theo}$) assuming deposition of a perfectly cylindrical filament. Layer heights were calculated using $H = \sqrt{\pi/4} * D_{fil,\ theo}$, determined experimentally in order to achieve excellent substrate adhesion. Interfilament separation distances (*IF*) were determined experimentally using $IF = 1.075 * D_{fil,theo}$. If this spacing between filaments was too large, poor-interfilament adhesion results in premature delamination during handling and/or straining. In contrast, if the spacing was too small, the unidirectional nanostructural alignment was disrupted, resulting in a significant deviation from the intended programmed material properties (Figures S19–S21, Supporting Information). By defining these key print parameters as functions of the programmed filament diameter, they were generalizable and consistent across the range of nozzle sizes and draw ratios accessed in this study.

3D printed samples were annealed on a hot plate set to 150 °C for 10 min (Figure S22, Supporting Information) with a constant flow of N_2 to prevent oxidative degradation. During annealing, samples were arranged on ⅛″ glass sheets coated with a thin layer of silicone oil (Beantown chemical) to prevent the samples from adhering to the glass. Multi-layered samples were annealed in a 150 °C oven for 1 h and did not exhibit detrimental shape distortion. Annealing time and temperature conditions were chosen in order to allow for the relaxation of trapped stresses and associated nanostructure rearrangement without significant loss of programmed geometry. For the SEBS studied, 150 °C was chosen as this temperature allowed for a rapid equilibration of material properties and nanostructure rearrangement (Figure S22, Supporting Information), without leading to measurable sample deformation, owing to the yield stress in the melt state. When expanding this process to a wider range of TPEs, specifically those of higher MW in which dynamics will be significantly hindered, thermal annealing conditions should be selected in which the material both maintains a sufficient yield stress and therefore will not exhibit significant deformation or flow and undergoes nanostructural relaxations and rearrangements to reach a plateau in properties on an acceptable timescale.

Structural Characterization: Small angle X-ray scattering was performed under vacuum at the 12-ID beamline at Brookhaven National Laboratory using a micro-focused (2 µm × 25 µm) 14.5 keV X-ray beam using 0.5 s collection times. Line profile scans were performed across individual printed filaments in a "top-down" orientation with a scan spacing of 5 µm. For the analysis presented in this work, all scans collected for each sample were summed to produce a single scattering pattern representing the average sample properties. Data processing was performed using custom Python scripts and the SMI beamline package. Background subtraction was performed to account for instrumental and environmental background. Orientational order parameters $<P_2>$ were calculated for each sample using the azimuthal scattering intensity profile for the primary scattering peak (0.025–0.04 $Å^{-1}$) (Figure S23, Supporting Information).[61,62,83] All values extracted from SAXS analyses represent the average and standard deviation taken from 3 replicate samples. Additional SAXS experiments included in the SI were performed on a Xeuss 3.0 with a Dectris Euger 2R 1M detector using a 1750 mm sample to detector distance and a Cu Kα (1.54 $Å^{-1}$) source using the high-resolution collimation setting and line-eraser mode. Azimuthal and radial intensity profiles were extracted using the XSACT software and were analyzed further using the same scripts as above.

Transmission Electron Microscopy: To prepare samples for TEM characterization, the 3DP filaments of interest were first sputter coated with a thin (≈10 nm) iridium layer to improve visibility during embedding and microtoming. Next, the samples were embedded in the desired orientation in a rigid fixative (EpoxiCure 2 Resin & Hardener) for mechanical support during slicing. After the epoxy was fully cured (24+ hrs), block faces were shaped using double-edged razors to expose the desired area of the filament, followed by collections of 40 nm (side-on orientation) or 80 nm (end-on orientation) cross-sections via cryo-ultramicrotomy (Leica Ultracut UCT Ultramicrotome) at a sample temperature of −65 °C with a −60 °C diamond knife temperature (Figure S24, Supporting Information). The cut specimens were dry-lifted and transferred to TEM grids (300 mesh, with an amorphous carbon layer). To provide electron contrast during imaging, preferential ruthenium tetroxide (RuO_4) staining of polystyrene domains was performed using a custom-made poly(methyl methacrylate) vapor chamber following previously published procedures.[84] Vapor-phase ruthenium tetroxide was generated from an aqueous solution by combining 10 mL DI water, 15 mg ruthenium dioxide, and 250 mg sodium metaperiodate. Vapor was allowed to accumulate within the chamber for ≈5 min prior to sample addition. Based on a time series ranging from 5–60 min, 15 min of exposure was found to provide optimal staining conditions and was used for all imaging. Upon removal of the TEM samples, the generator bath was quenched by adding 400 mg of sodium bisulfite. TEM imaging of the stained cryo-ultramicrotomed cross-sections was performed with a Talos L120C G2 Transmission Electron Microscope operated at 120 kV. An isotropic SEBS control sample was prepared and imaged similarly to validate sample preparation procedures (Figure S25, Supporting Information).

Mechanical Characterization: Tensile testing was performed on an Instron 5965 equipped with a 500 N load cell. Single filament samples for mechanical analysis were mounted in epoxy pucks with cyanoacrylate adhesive. Single filament sample gauge lengths varied between 20 – 40 mm. Measurements performed on single-layer 3D printed sheets and isotropic controls were tested using an ASTM 1708 standard dogbone geometry (17.5 mm × 5 mm gauge dimensions). During all tensile testing, the strain was applied at 100% min^{-1} to a maximum strain of 100%. Reported small strain modulus values were extracted from the small strain (0–2%) region (Figure S26, Supporting Information) and represent averages and standard deviations over 3–5 replicates. Dynamic mechanical analysis was performed on a Perkin Elmer DMA-8000 using the single-cantilever geometry at room temperature with an oscillation frequency of 1 s^{-1}, using 3D printed samples of appropriate dimensions (≈3.5 mm × 5.5 mm × 15 mm).

Supporting Information

Supporting Information is available from the Wiley Online Library or from the author.

Acknowledgements

The authors gratefully acknowledge Lutz Wiegart, Patryk Wasik, and Mikhail (Misha) Zhernenkov for their valuable assistance at NSLS-II. This research used beamline 12-ID of the National Synchrotron Light Source II, a U.S. Department of Energy (DOE) Office of Science User Facility operated for the DOE Office of Science by Brookhaven National Laboratory under Contract No. DE-SC0012704. The authors acknowledge the use of Princeton's Imaging and Analysis Center (IAC), which is partially supported by the Princeton Center for Complex Materials (PCCM), a National Science Foundation (NSF) Materials Research Science and Engineering Center (MRSEC; DMR-2011750). The authors also gratefully acknowledge support from Princeton PCCM SEED funds (MRSEC DMR-1420541). In addition, the authors acknowledge the support of Princeton Project X Innovation Funds. The authors would like to thank Kraton for providing the polymer used in this study, and M. R. Ivancevic for synthesizing and providing the chromophore used in this study. The authors would also like to thank Prof. R.A. Register for helpful conversation regarding thermoplastic elastomers, Clement Chan for assistance with NMR and helpful discussion regarding SAXS analysis, the Priestley laboratory for generously allowing use of their DSC and hot press, the Prudhomme lab for use of their ruthenium staining chamber, Sahana Sundar for assistance with TEM

sample preparation, as well as undergraduates Ariana Rausch and Daniel Simone for contributing to the development of Python code used to coordinate toolpath and extrusion during printing.

Conflict of Interest

The authors declare no conflict of interest.

Author Contributions

E.C.D. and A.S.F. conceived of and designed the research project. A.S.F. performed all 3D printing, sample characterization, and data analysis. A.S.F., E.C.D., and B.H.G. designed the extruder. B.H.G. built the extruder and developed custom Python scripts to enable 3D printing with the custom extruder. S.M.M. conducted DSC experiments, Linkam temperature calibrations, and cryo-microtomy, and assisted A.S.F. with DMA and TEM experiments. E.C.O. conducted rheological experiments and assisted A.S.F. with TEM experiments. A.S.F. and E.C.D. wrote the manuscript. All authors reviewed and approved the final manuscript.

Data Availability Statement

The data that support the findings of this study are available from the corresponding author upon reasonable request.

Keywords

3D printing, flow-induced alignment, hierarchical structures, thermoplastic elastomers

Received: July 4, 2024
Revised: August 31, 2024
Published online: September 24, 2024

[1] A. R. Studart, *Adv. Funct. Mater.* **2013**, *23*, 4423.
[2] J. Wei, F. Pan, H. Ping, K. Yang, Y. Wang, Q. Wang, Z. Fu, *Research* **2023**, *6*, 0164.
[3] Y. Man, G. Ding, L. Xudong, K. Xue, D. Qu, Z. Xie, *J. Asian Ceramic Soc.* **2021**, *9*, 1377.
[4] S. B. Darling, *Prog. Polym. Sci.* **2007**, *32*, 1152.
[5] K. M. Herbert, H. E. Fowler, J. M. McCracken, K. R. Schlafmann, J. A. Koch, T. J. White, *Nat. Rev. Mater.* **2022**, *7*, 23.
[6] C. L. C. Chan, J. M. Taylor, E. C. Davidson, *Nat. Synth* **2022**, *1*, 592.
[7] Q. Chen, P. F. Cao, R. C. Advincula, *Adv. Funct. Mater.* **2018**, *28*, 1800631.
[8] D. Mistry, N. A. Traugutt, B. Sanborn, R. H. Volpe, L. S. Chatham, R. Zhou, B. Song, K. Yu, K. N. Long, C. M. Yakacki, *Nat. Commun.* **2021**, *12*, 6677.
[9] E. B. Trigg, N. S. Hmeidat, L. M. Smieska, A. R. Woll, B. G. Compton, H. Koerner, *Addit. Manuf.* **2021**, *37*, 101729.
[10] S. Gantenbein, K. Masania, W. Woigk, J. P. W. Sesseg, T. A. Tervoort, A. R. Studart, *Nature* **2018**, *561*, 226.
[11] B. B. Patel, D. J. Walsh, D. H. Kim, J. Kwok, B. Lee, D. Guironnet, Y. Diao, *Sci. Adv.* **2020**, *6*, eaaz7202.
[12] E. C. Davidson, A. Kotikian, S. Li, J. Aizenberg, J. A. Lewis, *Adv. Mater.* **2020**, *32*, 1905682.
[13] B. M. Boyle, T. A. French, R. M. Pearson, B. G. McCarthy, G. M. Miyake, *ACS Nano* **2017**, *11*, 3052.
[14] M. Cai, S. Nie, Y. Du, C. Wang, J. Song, *ACS Appl. Mater. Interfaces* **2019**, *11*, 14340.
[15] S. Jiang, X. Liu, J. Liu, D. Ye, Y. Duan, K. Li, Z. Yin, Y. Huang, *Adv. Mater.* **2022**, *34*, 2200070.
[16] S. M. Montgomery, X. Kuang, C. D. Armstrong, H. J. Qi, *Curr. Opin. Solid State Mater. Sci.* **2020**, *24*, 100869.
[17] M. J. Mirzaali, S. Janbaz, M. Strano, L. Vergani, A. A. Zadpoor, *Sci. Rep.* **2018**, *8*, 965.
[18] Y. Jiang, Q. Wang, *Sci. Rep.* **2016**, *6*, 34147.
[19] A. Mohammadi, E. Hajizadeh, Y. Tan, P. Choong, D. Oetomo, *Int. J. Bioprint* **2023**, *9*, 696.
[20] L. Cappello, K. C. Galloway, S. Sanan, D. A. Wagner, R. Granberry, S. Engelhardt, F. L. Haufe, J. D. Peisner, C. J. Walsh, *Soft Rob.* **2018**, *5*, 662.
[21] A. Pal, V. Restrepo, D. Goswami, R. V. Martinez, *Adv. Mater.* **2021**, *33*, 2006939.
[22] F. Vanneste, O. Goury, J. Martinez, S. Lefebvre, H. Delingette, C. Duriez, *IEEE Robot. Autom. Lett.* **2020**, *5*, 2380.
[23] B. G. Compton, J. A. Lewis, *Adv. Mater.* **2014**, *26*, 5930.
[24] J. J. Martin, B. E. Fiore, R. M. Erb, *Nat. Commun.* **2015**, *6*, 8641.
[25] D. Kokkinis, M. Schaffner, A. R. Studart, *Nat. Commun.* **2015**, *6*, 8643.
[26] A. Kotikian, R. L. Truby, J. W. Boley, T. J. White, J. A. Lewis, *Adv. Mater.* **2018**, *30*, 1706164.
[27] B. Peng, Y. Yang, T. Ju, K. A. Cavicchi, *ACS Appl. Mater. Interfaces* **2021**, *13*, 12777.
[28] T. H. Ware, J. S. Biggins, A. F. Shick, M. Warner, T. J. White, *Nat. Commun.* **2016**, *7*, 10781.
[29] A. N. Semenov, *Macromolecules* **1993**, *26*, 6617.
[30] L. Leibler, *Macromolecules* **1980**, *13*, 1602.
[31] G. H. Fredrickson, F. S. Bates, *Annu. Rev. Mater. Sci.* **1996**, *26*, 501.
[32] F. S. Bates, G. H. Fredrickson, *Annu. Rev. Phys. Chem.* **1990**, *41*, 525.
[33] M. J. Folkes, A. Keller, *Polymer* **1971**, *12*, 222.
[34] A. P. Marencic, R. A. Register, *Annu. Rev. Chem. Biomol. Eng.* **2010**, *1*, 277.
[35] S. Ji, U. Nagpal, G. Liu, S. P. Delcambre, M. Müller, J. J. de Pablo, P. F. Nealey, *ACS Nano* **2012**, *6*, 5440.
[36] G. Hadziioannou, A. Mathis, A. Skoulios, *Colloid & Polymer Sci* **1979**, *257*, 136.
[37] A. Keller, E. Pedemonte, F. M. Willmouth, *Kolloid-Z.u.Z.Polymere* **1970**, *238*, 385.
[38] R. Mao, E. M. McCready, W. R. Burghardt, *Soft Matter* **2014**, *10*, 6198.
[39] H. H. Lee, R. A. Register, D. A. Hajduk, S. M. Gruner, *Polym. Eng. Sci.* **1996**, *36*, 1414.
[40] R. J. Albalak, E. L. Thomas, *J. Polym. Sci., Part B: Polym. Phys.* **1993**, *31*, 37.
[41] I. W. Hamley, *J. Phys.: Condens. Matter* **2001**, *13*, R643.
[42] R. G. C. Arridge, M. J. Folkes, *J. Phys. D: Appl. Phys.* **1972**, *5*, 344.
[43] J. A. Odell, A. Keller, *Polym. Eng. Sci.* **1977**, *17*, 544.
[44] A. Skoulios, *J. Polym. Sci.: Polym. Symp.* **1977**, *58*, 369.
[45] E. V. Gouinlock, R. S. Porter, *Polym. Eng. Sci.* **1977**, *17*, 535.
[46] I. Yamaoka, M. Kimura, *Polymer* **1993**, *34*, 4399.
[47] C. C. Honeker, E. L. Thomas, *Chem. Mater.* **1996**, *8*, 1702.
[48] C. Daniel, I. W. Hamley, K. Mortensen, *Polymer* **2000**, *41*, 9239.
[49] R. J. Albalak, E. L. Thomas, M. S. Capel, *Polymer* **1997**, *38*, 3819.
[50] R. J. Albalak, M. S. Capel, E. L. Thomas, *Polymer* **1998**, *39*, 1647.
[51] M. A. Villar, D. R. Rueda, F. Ania, E. L. Thomas, *Polymer* **2002**, *43*, 5139.
[52] Z. R. Chen, J. A. Kornfield, S. D. Smith, J. T. Grothaus, M. M. Satkowski, *Science* **1997**, *277*, 1248.
[53] Z. R. Chen, J. A. Kornfield, *Polymer* **1998**, *39*, 4679.
[54] A. Manthis, G. Hadziioannou, A. Skoulios, *Polym. Eng. Sci.* **1977**, *17*, 570.
[55] S. Pujari, M. A. Keaton, P. M. Chaikin, R. A. Register, *Soft Matter* **2012**, *8*, 5358.
[56] K. Koppi, M. Tirrell, F. Bates, K. Almdal, R. Colby, *J. de Physiq. II* **1992**, *2*, 1941.

[57] F. Morrison, G. L.e Bourvellec, H. H. Winter, *J. Appl. Polym. Sci.* **1987**, *33*, 1585.
[58] J. W. Boley, K. Chaudhary, T. J. Ober, M. Khorasaninejad, W. T. Chen, E. Hanson, A. Kulkarni, J. Oh, J. Kim, L. K. Aagesen, A. Y. Zhu, F. Capasso, K. Thornton, P. V. Braun, J. A. Lewis, *Adv. Mater.* **2017**, *29*, 1604778.
[59] C. Duty, C. Ajinjeru, V. Kishore, B. Compton, N. Hmeidat, X. Chen, P. Liu, A. A. Hassen, J. Lindahl, V. Kunc, *J. Manuf. Processes* **2018**, *35*, 526.
[60] C. D. Han, D. A. Rao, *J. Appl. Polym. Sci.* **1979**, *24*, 225.
[61] R. J. Roe, *J. Polym. Sci. Part A-2: Polym. Phys.* **1970**, *8*, 1187.
[62] G. J. Vancso, *Polym. Bull.* **1990**, *24*, 233.
[63] C. C. Honeker, E. L. Thomas, R. J. Albalak, D. A. Hajduk, S. M. Gruner, M. C. Capel, *Macromolecules* **2000**, *33*, 9395.
[64] T. Pakula, K. Saijo, H. Kawai, T. Hashimoto, *Macromolecules* **1985**, *18*, 1294.
[65] R. T. Myers, R. E. Cohen, A. Bellare, *Macromolecu.* **1999**, *32*, 2706.
[66] S. Bourrigaud, G. Marin, V. Dabas, C. Dupuy, D. Silagy, *Polym. Eng. Sci.* **2006**, *46*, 372.
[67] M. M. Denn, *Annu. Rev. Fluid Mech.* **1980**, *12*, 365.
[68] M. A. Matovich, J. R. A. Pearson, *Ind. Eng. Chem. Fund.* **1969**, *8*, 512.
[69] C. McIlroy, P. D. Olmsted, *J. Rheology* **2017**, *61*, 379.
[70] E. M. McCready, W. R. Burghardt, *Macromolecules* **2015**, *48*, 264.
[71] E. M. McCready, W. R. Burghardt, *J. Rheology* **2015**, *59*, 935.
[72] R. Xie, S. Mukherjee, A. E. Levi, J. L. Self, H. Wang, M. L. Chabinyc, C. M. Bates, *Macromolecules* **2021**, *54*, 5636.
[73] R. Xie, S. Mukherjee, A. E. Levi, V. G. Reynolds, H. Wang, M. L. Chabinyc, C. M. Bates, *Sci. Adv.* **2020**, *6*, eabc6900.
[74] M. R. Ivancevic, J. A. Wisch, D. J. Oblinsky, M. D. Ogbaje, A. S. Fergerson, E. C. Davidson, C. Risko, G. D. Scholes, B. P. Rand, Q. C. Burlingame, Y. L. Loo, n.d.
[75] N. A. Patil, K. Joshi, J. Lee, K. E. Strawhecker, R. Dunn, T. Lawton, E. D. Wetzel, J. H. Park, *Addit. Manuf.* **2024**, *82*, 104044.
[76] Y. Cohen, R. J. Albalak, B. J. Dair, M. S. Capel, E. L. Thomas, *Macromolecules* **2000**, *33*, 6502.
[77] B. Yang, A. M. Nasab, S. J. Woodman, E. Thomas, L. G. Tilton, M. Levin, R. Kramer-Bottiglio, *Adv. Mater.* **2024**, *36*, 2400241.
[78] J. S. A. Ishibashi, J. A. Kalow, *ACS Macro Lett.* **2018**, *7*, 482.
[79] J. Z. Zhao, T. J. Yue, B. H. Ren, X. B. Lu, W. M. Ren, *Nat. Commun.* **2024**, *15*, 3002.
[80] B. Qin, S. Liu, Z. Huang, L. Zeng, J. F. Xu, X. Zhang, *Nat. Commun.* **2022**, *13*, 7595.
[81] T. O. Machado, C. J. Stubbs, V. Chiaradia, M. A. Alraddadi, A. Brandolese, J. C. Worch, A. P. Dove, *Nature* **2024**, *629*, 1069.
[82] Z. Chen, M. Yang, M. Ji, X. Kuang, H. J. Qi, T. Wang, *Mater. Des.* **2021**, *197*, 109189.
[83] M. T. Sims, L. C. Abbott, R. M. Richardson, J. W. Goodby, J. N. Moore, *Liq. Cryst.* **2019**, *46*, 11.
[84] B. K. Wilson, R. K. Prud'homme, *J. Colloid Interface Sci.* **2021**, *604*, 208.